

# Molecular bases of the interactions of ATG16L1 with FIP200 and ATG8 family proteins

Received: 9 September 2024

Accepted: 8 September 2025

Published online: 10 October 2025

Xinyu Gong<sup>1,3</sup>, Yuqian Zhou<sup>1,3</sup>, Yingli Wang<sup>1</sup>, Yubin Tang<sup>1</sup>, Haobo Liu<sup>1</sup>, Xindi Zhou<sup>1</sup>, Yuchao Zhang<sup>1</sup>, Hanbo Guo<sup>1</sup>, Zhenpeng Guo<sup>1</sup> & Lifeng Pan<sup>1,2</sup>✉

Macroautophagy maintains cellular and organismal homeostasis, and entails de novo synthesis of double-membrane autophagosome. The effective formation of autophagosome requires the recruitment of the ATG12-ATG5-ATG16L1 complex to the pre-autophagosomal structure by relevant ATG16L1-binding autophagic factors including FIP200. However, the molecular mechanism governing the specific interaction of ATG16L1 with FIP200 remains elusive. Here, we uncover that ATG16L1 contains a FIP200-interacting region (FIR), which not only can directly bind FIP200 Claw domain, but also can serve as an atypical ATG8-interacting motif to selectively recognize mammalian ATG8 family proteins (ATG8s). We determine the high-resolution crystal structures of ATG16L1 FIR in complex with FIP200 Claw and GABARAPL1, respectively, and elucidate the molecular mechanism underlying the interactions of ATG16L1 with FIP200 and ATG8s. To distinguish the precise contribution of FIP200 from ATG8s for binding to ATG16L1 FIR in autophagy, we develop a ATG16L1 mutant that can exclusively interact with ATG8s but not FIP200. Finally, using relevant cell-based functional assays, we demonstrate that the interaction of ATG16L1 with FIP200 is indispensable for the effective autophagic flux. In conclusion, our findings provide mechanistic insights into the interactions of ATG16L1 with FIP200 and ATG8s, and are valuable for further understanding the function of ATG16L1 in autophagy.

Macroautophagy (hereafter referred to as autophagy) is a well-conserved and lysosome-dependent catabolic process that recycles undesired or harmful cytosolic components for providing essential building blocks to maintain cellular homeostasis in mammals<sup>1–4</sup>. Autophagy necessitates de novo synthesis of double-membrane autophagosome through the sophisticated cooperation of a series of autophagy-related (ATG) proteins<sup>3,5,6</sup>. During the amino acid starvation-induced canonical autophagy, calcium transients trigger liquid-liquid phase separation of FAK family kinase-interacting protein of 200 kDa (FIP200) and the FIP200-containing Unc-51-like

kinase (ULK) complex in the pre-autophagosomal structure (PAS) to initiate autophagosome formation<sup>7</sup>. Concurrently, the class III phosphatidylinositol-3-kinase complex I (PI3KC3-C1) is translocated to the PAS and is subsequently activated to phosphorylate phosphatidylinositol (PI) to generate phosphatidylinositol-3-phosphate (PI3P)<sup>8</sup>. Meanwhile, both the FIP200 subunit of the ULK complex and the WD repeat domain phosphoinositide-interacting protein 2 (WIPI2) that senses the PI3P signal from PI3KC3-C1 can regulate the targeting of the E3-like ATG12-ATG5-ATG16L1 complex (the ATG16L1 complex) to the PAS<sup>9–12</sup>. Subsequently, the ATG16L1 complex

<sup>1</sup>State Key Laboratory of Chemical Biology, Shanghai Institute of Organic Chemistry, University of Chinese Academy of Sciences, Chinese Academy of Sciences, Shanghai, China. <sup>2</sup>School of Chemistry and Materials Science, Hangzhou Institute for Advanced Study, University of Chinese Academy of Sciences, Hangzhou, China. <sup>3</sup>These authors contributed equally: Xinyu Gong, Yuqian Zhou. ✉e-mail: [panlf@sioc.ac.cn](mailto:panlf@sioc.ac.cn)

catalyzes the phosphatidylethanolamine (PE) lipidation of ATG8 family proteins to facilitate the elongation of PAS to form autophagosome<sup>13–15</sup>. Although the molecular mechanism underpinning the recruitment of the ATG16L1 complex by WIPI2 is well elucidated in previous studies<sup>12,16</sup>, how FIP200 specifically interacts with ATG16L1 to recruit the ATG16L1 complex remains elusive. Moreover, why autophagy deploys two distinct approaches to recruit the ATG16L1 complex is still enigmatic.

In addition to non-selective canonical autophagy, accumulating studies have uncovered considerable selective autophagy processes mediated by different types of autophagy receptors<sup>17–23</sup>. Currently identified autophagy receptors in mammals, such as p62, NBR1, Optineurin, CCPG1, NDP52, and TAX1BP1, all encompass a cargo-associating domain that can specially recognize certain types of autophagic cargoes as well as a distinct ATG8-interacting motif (AIM) that recognizes the ATG8 family proteins known as LC3A, LC3B, LC3C, GABARAP, GABARAPL1, and GABARAPL2 in mammals<sup>19,20,24–26</sup>. Moreover, recent studies revealed that in order to induce *in situ* autophagosome formation to envelope and sequester the targeting cargoes, many autophagy receptors can directly interact with FIP200 to recruit the ULK complex<sup>27–30</sup>. Particularly, some autophagy receptors can directly bind to the Claw domain of FIP200 through their respective FIP200-interacting region (FIR) for recruiting the ULK complex<sup>27,28,30,31</sup>. Since the sequence pattern of AIM bears a striking resemblance to that of FIR, the AIM motifs of many autophagy receptors can also function as FIR to interact with FIP200 Claw<sup>27,28</sup>. However, due to the high similarity, it is challenging to dissect the individual contribution of FIP200 and ATG8 family proteins for binding to these autophagy receptors. Interestingly, similar to aforementioned autophagy receptors, mammalian ATG16L1 can function as an adapter to specifically recognize invading pathogens or pathogen-containing vacuoles through its C-terminal WD40 repeats domain to mediate the

antibacterial selective autophagy (also named as xenophagy)<sup>32–35</sup>. Moreover, a previous elegant study of the network organization of the human autophagy system well demonstrated that ATG16L1 can directly bind to ATG8 family proteins<sup>36</sup>. However, how ATG16L1 interacts with ATG8 family proteins and the detailed relationship between FIP200 and ATG8 family proteins in binding to ATG16L1 are largely unknown.

In this study, we discover that ATG16L1 contains a typical FIR motif for directly interacting with the Claw domain of FIP200. Importantly, in addition to binding to FIP200 Claw, ATG16L1 FIR can also serve as a noncanonical AIM motif to selectively recognize mammalian ATG8 family proteins. Moreover, our determined crystal structures of the ATG16L1 FIR/FIP200 Claw complex and the ATG16L1 FIR/GABARAPL1 complex not only uncover the detailed molecular mechanism governing the specific interactions of ATG16L1 with FIP200 and ATG8 family members, but also reveal that FIP200 and ATG8 family proteins are mutually exclusive in binding to ATG16L1. On this basis, we devise a specific ATG16L1 mutant that can interact well with ATG8 family proteins but not FIP200. Finally, using this ATG16L1 mutant together with relevant cell-based functional assays, we demonstrate that the interaction of ATG16L1 FIR with FIP200 is indispensable for the effective autophagic flux in canonical autophagy.

## Results

### Biochemical characterizations of the interaction of ATG16L1 with FIP200 Claw

Previous studies uncovered that the ATG16L1(229–242) region adjacent to the WIPI2-binding site 1 (WBS1) of ATG16L1 is essential for the interaction between ATG16L1 and FIP200 (Fig. 1a)<sup>9,10</sup>. Consistently, using size-exclusion chromatography (SEC)-based assays, we demonstrated that the highly conserved central region of ATG16L1, the ATG16L1(78–247) fragment (Supplementary Fig. 1), can readily interact

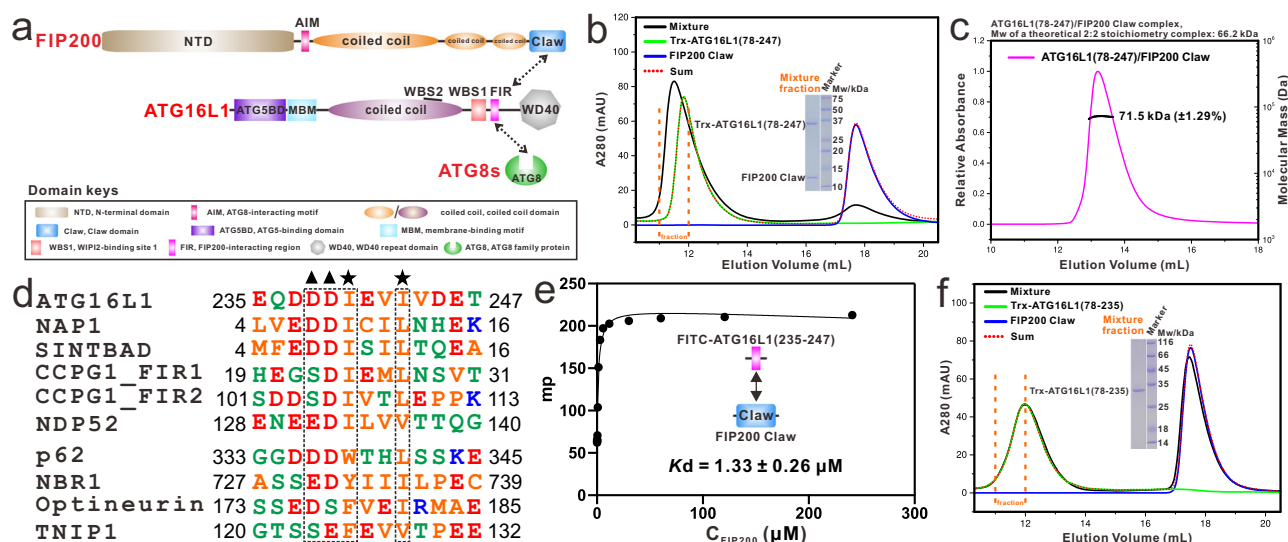


**Fig. 1 | Biochemical characterizations of the interaction of ATG16L1 with FIP200.** **a** A schematic diagram showing the domain organizations of FIP200, ATG16L1, and mammalian ATG8 family proteins. In this drawing, the interactions of ATG16L1 with FIP200 and mammalian ATG8 family proteins are highlighted and indicated by two-way arrows. **b** Size-exclusion chromatography-based analysis of the interaction of FIP200 Claw with Trx-tagged ATG16L1(78–247). In this panel, the “Sum” stands for the theoretical sum of Trx-tagged ATG16L1(78–247) and FIP200 Claw profiles, while “Mixture” stands for the Trx-tagged ATG16L1(78–247) and FIP200 Claw mixture sample. **c** Multi-angle light-scattering analysis of the purified ATG16L1(78–247)/FIP200 Claw complex showing the relative light-scattering signals as a function of elution volume. The molecular mass error is the fitted error obtained from the data analysis software. **d** Sequence alignment analysis of the FIR

of ATG16L1 with the currently known FIP200 Claw-binding regions of NAPI, SINTBAD, CCPG1, NDP52, p62, NBR1, Optineurin, and TNIP1 from the human species. In this alignment, the highly conserved acidic residues (Asp, Glu, or potentially phosphorylated Ser residue) and the following two conserved hydrophobic residues are boxed and highlighted with black triangles and stars, respectively. **e** The fluorescence polarization (FP)-based assay measuring the binding affinity of FIP200 Claw with FITC-labeled ATG16L1 FIR. The K<sub>d</sub> value is the fitted dissociation constant with standard errors obtained by using the one-site binding model to fit the FP data. **f** Size-exclusion chromatography-based analysis of the interaction of FIP200 Claw with Trx-tagged ATG16L1(78–235). In this panel, the “Sum” stands for the theoretical sum of Trx-tagged ATG16L1(78–235) and FIP200 Claw profiles, while “Mixture” stands for the Trx-tagged ATG16L1(78–235) and FIP200 Claw mixture sample.

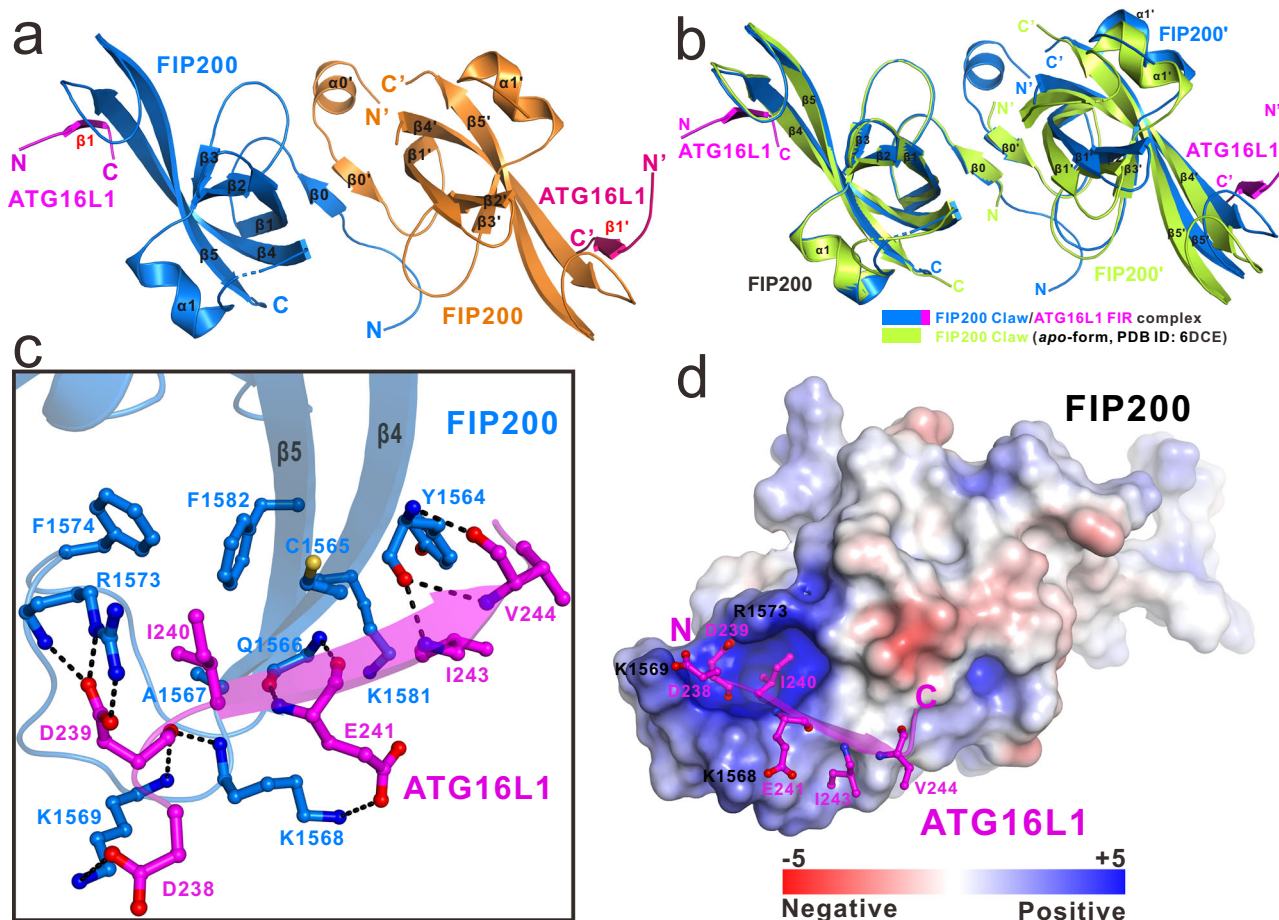


**Fig. 2 | The molecular mechanism of FIP200 and ATG16L1 interaction.** **a** Ribbon diagram showing the overall structure of the dimeric FIP200 Claw/ATG16L1 FIR complex. In this drawing, two FIP200 Claw molecules are colored in orange and marine, while two bound ATG16L1 FIR motifs are colored in magenta and hot pink, respectively. **b** Ribbon representation showing the structural comparison of *apo*-form FIP200 Claw dimer (green, PDB ID: 6DCE) with the FIP200 Claw/ATG16L1 FIR complex (blue/magenta). In this drawing, the two dimeric structures are overlaid by

aligning selected one FIP200 Claw monomer in these two structures. **c** Ribbon-stick model showing the detailed interactions between FIP200 Claw and ATG16L1 FIR. The hydrogen bonds and salt bridges involved in the interaction are shown as dotted lines. **d** The combined surface charge representation and the ribbon-stick model showing the charge-charge interactions between FIP200 Claw and ATG16L1 FIR in the solved complex structure.

with FIP200(1490–1594) (hereafter referred to as FIP200 Claw) (Fig. 1b). Further multi-angle light-scattering analysis revealed that the purified ATG16L1(78–247)/FIP200 Claw complex forms a stable 2:2 stoichiometric complex in solution (Fig. 1c). Strikingly, detailed sequence alignment analysis of the FIP200-binding region of ATG16L1 with that of NAP1, SINTBAD, CCPG1, NDP52, p62, NBR1, Optineurin and TNIP1, all of which were demonstrated to directly interact with FIP200 Claw<sup>27–31,37–40</sup>, unraveled that the ATG16L1(235–247) region conforms to the criteria for a FIP200 Claw-binding FIR motif<sup>27</sup>, likely representing a putative FIR motif (hereafter referred to as ATG16L1 FIR) (Fig. 1d). Indeed, further quantitative fluorescent polarization (FP)-based assay revealed that ATG16L1 FIR can specifically interact with FIP200 Claw with a *K<sub>d</sub>* value of about  $\sim 1.33 \mu\text{M}$  (Fig. 1e). In contrast, the removal of ATG16L1 FIR totally disrupted the association of ATG16L1(78–247) with FIP200 Claw (Fig. 1f). Taken together, all these data clearly demonstrated that ATG16L1 contains a conserved FIR motif to directly interact with the Claw domain of FIP200.

**The overall structure of the ATG16L1 FIR/FIP200 Claw complex** Then, we intended to determine the ATG16L1 FIR/FIP200 Claw complex structure to uncover how ATG16L1 FIR binds to the Claw domain of FIP200. After numerous attempts, we finally managed to solve the crystal structure of ATG16L1 FIR in complex with FIP200 Claw at 1.61 Å

resolution (Supplementary Table 1). The determined ATG16L1 FIR/FIP200 Claw complex structure is composed of two ATG16L1 FIR molecules and a FIP200 Claw dimer, forming a distinct 2:2 stoichiometric hetero-tetramer (Fig. 2a), in line with our aforementioned multi-angle light-scattering result (Fig. 1c). In the complex structure, except for a distinct N-terminal  $\alpha$ -helix that was only found in one of the two FIP200 Claw domains owing to crystal packing (Supplementary Fig. 2a), the two monomeric FIP200 Claw domains adopt a highly similar core architecture assembled by six  $\beta$ -strands and one  $\alpha$ -helix (Supplementary Fig. 2b). In parallel, the two ATG16L1 FIR molecules in the complex structure mainly form two short  $\beta$ -strands that symmetrically augment the  $\beta$ 4-strand of two FIP200 Claw domains in an anti-parallel manner (Fig. 2a). Further structural comparison analyses showed that the overall structure of the monomeric FIP200 Claw domain in the ATG16L1 FIR/FIP200 Claw complex is highly akin to that of the *apo*-form FIP200 Claw domain (PDB ID: 6DCE) (Supplementary Fig. 2c), whereas the binding of ATG16L1 FIR to FIP200 Claw induces an obvious conformational rearrangement of the FIP200 Claw dimer (Fig. 2b). Notably, similar phenomena were also observed in our previous studies<sup>27,31</sup>.

**The binding interface between ATG16L1 FIR and FIP200 Claw** In the ATG16L1 FIR/FIP200 Claw complex structure, each ATG16L1 FIR molecule packs extensively with a highly electropositive and

**Table 1 | The measured binding affinities between ATG16L1 FIR and FIP200 Claw, or their mutants, by FP-based binding assays**

ATG16L1	FIP200 Claw	K <sub>d</sub> (μM)
FIR	WT	1.33 ± 0.26
FIR	K1568A	34.46 ± 6.00
FIR	K1569A	32.87 ± 5.14
FIR	R1573E	343.59 ± 245.92
FIR	F1574Q	61.38 ± 11.79

hydrophobic concave groove that is situated adjacent to the β4/β5 connecting region of the monomeric FIP200 Claw, burying a total interface area of ~505 Å<sup>2</sup> (Fig. 2a). Further careful analyses of the molecular interface in the ATG16L1 FIR/FIP200 Claw complex structure revealed that the hydrophobic side chain of ATG16L1 I240 deeply inserts into a hydrophobic pocket formed by the hydrophobic side chains of C1565, A1567, F1574, and F1582 residues together with the aliphatic side chain group of R1573 residue of FIP200 Claw (Fig. 2c and Supplementary Fig. 2d), and concurrently, the hydrophobic side chains of ATG16L1 I243 and V244 residues form hydrophobic contacts with the aromatic side chain of Y1564 and the aliphatic side chain group of K1581 from FIP200 (Fig. 2c). Furthermore, the negatively charged D238, D239 and E241 residues of ATG16L1 FIR form specific hydrogen bonding and charge-charge interactions with the positively charged K1569, R1573, and K1568 residues of FIP200 Claw (Fig. 2c, d). In addition, the backbone groups of E241, I243, and V244 residues of ATG16L1 FIR couple with the backbone groups of Q1566 and Y1564 residues of FIP200 to form five specific backbone hydrogen bonds (Fig. 2c). In keeping with their critical structural roles, all these key binding interface residues of ATG16L1 and FIP200 are highly conserved in different eukaryotic species (Supplementary Figs. 1 and 3). Consistent with our structural results, further FP-based assays showed that point mutations of key interface residues of FIP200 Claw, such as the K1568A, K1569A, R1573E, and F1574Q mutations, all significantly decrease the specific interaction of FIP200 Claw with ATG16L1 FIR (Table 1 and Supplementary Fig. 4). Reciprocally, point mutations of key interface residues from ATG16L1 FIR, including the D238R, D239R, I240Q, E241R, and I243Q mutations of ATG16L1 FIR, all largely attenuate or essentially disrupt the interaction between FIP200 Claw and ATG16L1 FIR (Supplementary Fig. 5). Therefore, all those mutagenesis-based biochemical assays confirmed the specific interaction between ATG16L1 FIR and FIP200 Claw observed in the solved ATG16L1 FIR/FIP200 Claw complex structure.

### Biochemical characterizations of the interactions of ATG16L1 with ATG8 family proteins

Since the reported FIR motifs have been demonstrated to directly engage with mammalian ATG8 family proteins<sup>27,31</sup>, we suspected that ATG16L1 FIR may also recognize mammalian ATG8 orthologs. Indeed, our ITC analyses revealed that ATG16L1 FIR can directly interact with six mammalian ATG8 members, and preferentially binds to GABARAPL1 and LC3C with a K<sub>d</sub> value of ~4.59 μM and ~6.27 μM, respectively (Fig. 3a, f and Supplementary Fig. 6). Then, we chose GABARAPL1 as a representative to further characterize the binding mechanism of ATG16L1 FIR with ATG8 family proteins. Our SEC results showed that the FIR-containing ATG16L1(78–247) and ATG16L1(235–247) fragments can readily interact with GABARAPL1 (Supplementary Fig. 7a, b). In contrast, the ATG16L1(78–235) fragment, which lacks the FIR motif of ATG16L1, is completely unable to interact with GABARAPL1 (Supplementary Fig. 7c). Concurrently, we also utilized NMR to validate the interaction between GABARAPL1 and ATG16L1. Titrations of <sup>15</sup>N-labeled GABARAPL1 with un-labeled ATG16L1(235–247) or ATG16L1(78–247) proteins showed that many peaks in the <sup>1</sup>H-<sup>15</sup>N HSQC

spectra of GABARAPL1 undergo significant chemical shift changes or peak-broadenings, confirming that the FIR motif-containing ATG16L1 fragments can directly bind to GABARAPL1 (Supplementary Fig. 8). Taken together, all these data clearly demonstrated that ATG16L1 FIR can function as an unconventional AIM motif to directly recognize mammalian ATG8 orthologs.

### The structure of ATG16L1 FIR in complex with GABARAPL1

To further uncover the detailed molecular mechanism underlying the selective recognitions of ATG8 family proteins by ATG16L1 FIR, we determined the high-resolution crystal structure of GABARAPL1 in complex with ATG16L1 FIR (Supplementary Table 1). In the determined GABARAPL1/ATG16L1 FIR complex structure, GABARAPL1 adopts a typical ATG8 family protein architecture assembled by a ubiquitin-like structural core and two preceding N-terminal α-helices (Fig. 3b). In the complex structure, the clearly defined ATG16L1 FIR motif contains 10 highly conserved residues spanning from Q236 to D245 of ATG16L1 (Supplementary Fig. 9a), and adopts an extended configuration to occupy the canonical AIM-binding groove of GABARAPL1, which is mainly formed by the β1-strand, β2-strand, α2-helix and α3-helix of GABARAPL1 (Fig. 3b, c). Further structural analyses of the binding interface of the GABARAPL1/ATG16L1 FIR complex revealed that the interaction between GABARAPL1 and ATG16L1 FIR is mainly mediated by both polar and hydrophobic interactions (Fig. 3c). In particular, the negatively charged side chains of ATG16L1 D239, E241 interact with the positively charged side chains of K48, K46 and R67 of GABARAPL1 to form three charge-charge interactions, and the backbone amide and oxygen groups of ATG16L1 E241 together with the backbone amide group of ATG16L1 I243 form three backbone hydrogen bonds with the GABARAPL1 K48 and L50 residues (Fig. 3c, d). In addition, the GABARAPL1/ATG16L1 FIR interaction is further strengthened by four specific hydrogen bonds, two of which are formed between the backbone oxygen groups of D238 and I240 residues of ATG16L1 and the positively charged side chain of GABARAPL1 K46, while the other two are mediated by the backbone oxygen group of ATG16L1 I243 and the positively charged side chain of GABARAPL1 R28 (Fig. 3c). In parallel, the hydrophobic side chains of ATG16L1 I240 and V242 residues pack against a hydrophobic groove of GABARAPL1 formed by the hydrophobic side chains of I21, P30, L50, F104 and the aliphatic portion of the side chain of GABARAPL1 K48 residue (Fig. 3c, e). Moreover, the hydrophobic side chain of ATG16L1 I243 occupies a hydrophobic pocket assembled by the side chains of Y49, V51, P52, L55, F60, and L63 residues of GABARAPL1 (Fig. 3c, e). Consistently, all these key binding interface residues of ATG16L1 FIR and GABARAPL1 are highly conserved during evolution (Supplementary Figs. 1 and 10). Using ITC-based assays, we further verified the specific interactions between interface residues of GABARAPL1 and ATG16L1 FIR observed in the complex structure. Individual point mutations of key residues involved in the binding interface of GABARAPL1/ATG16L1 FIR complex either from GABARAPL1 or ATG16L1 FIR, such as the I21Q, K48E, L50Q and R67E mutations of GABARAPL1 (Table 2 and Supplementary Fig. 11), or the D239R, I240Q, E241R, V242E and I243Q mutations of ATG16L1 FIR (Table 2 and Supplementary Fig. 12), all dramatically decrease or essentially disrupt the association of GABARAPL1 with ATG16L1 FIR. Meanwhile, based on the previous backbone assignment of GABARAPL1 (BMRB Entry 17412)<sup>41</sup>, we assigned the NMR peaks in the <sup>1</sup>H-<sup>15</sup>N HSQC spectrum of the <sup>15</sup>N-labeled GABARAPL1 and quantified the relevant chemical shift changes in our NMR titration experiments (Supplementary Figs. 8a and 13a). Further mapping the chemical shift differences onto our crystal structure of the GABARAPL1/ATG16L1 FIR complex revealed that the significant backbone amide chemical shift changes are only rich in the ATG16L1 FIR-binding regions of GABARAPL1 (Supplementary Fig. 13b), confirming that ATG16L1 FIR binds to the canonical AIM-binding sites of GABARAPL1 in solution. Notably, previous studies showed that the core unconventional AIM motif of

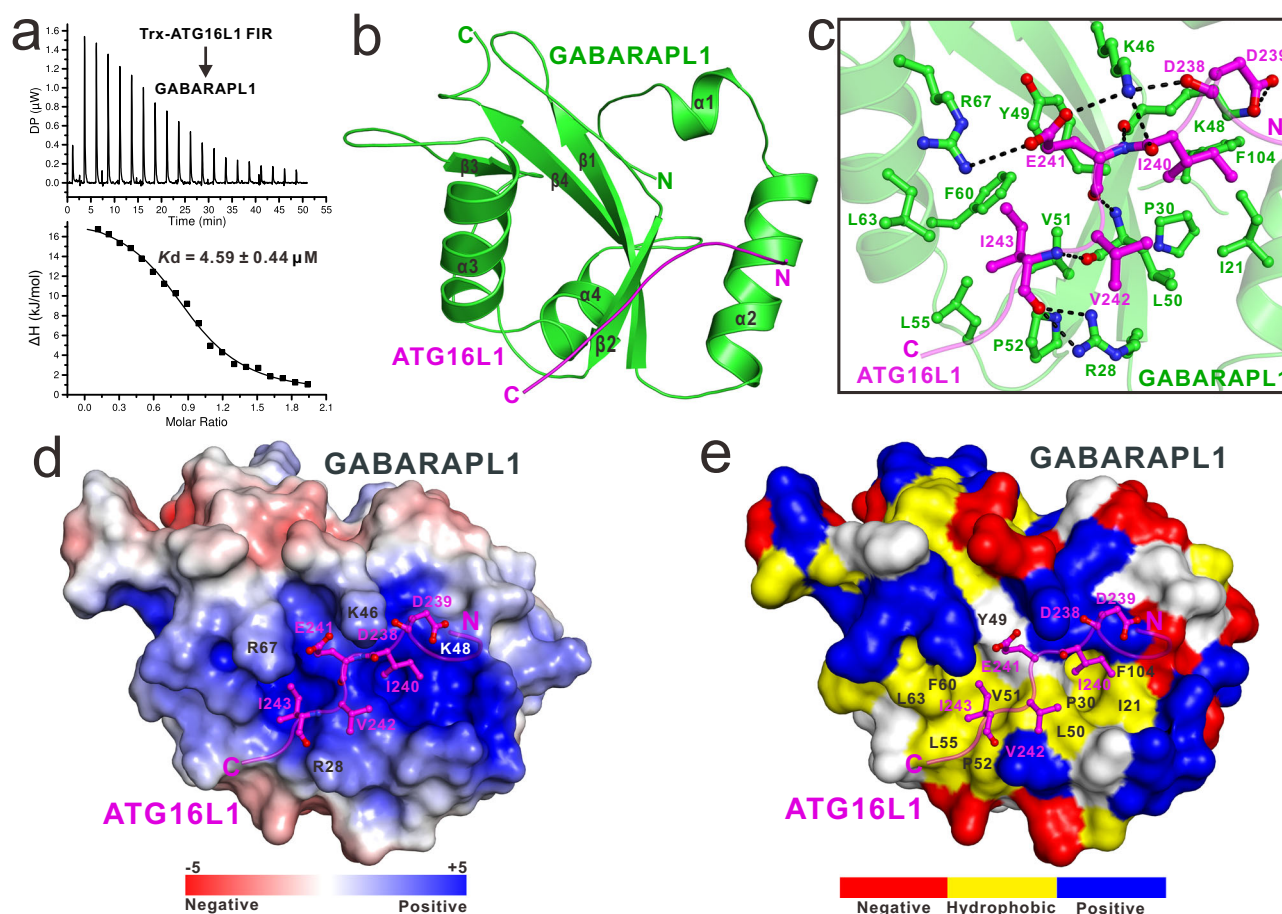


**Fig. 3 | Biochemical and structural characterizations of the interactions of ATG16L1 FIR with mammalian ATG8 family proteins.** **a** ITC-based measurement of the binding affinity of GABARAPL1 with Trx-tagged ATG16L1 FIR. **b** Ribbon diagram showing the overall structure of the GABARAPL1/ATG16L1 FIR complex. In this drawing, the GABARAPL1 molecule is colored in green, while ATG16L1 FIR in magenta. **c** The ribbon-stick model showing the detailed interactions between GABARAPL1 and ATG16L1 FIR. The hydrogen bonds and salt bridges involved in the interaction are shown as dotted lines. **d** The combined surface charge representation and the ribbon-stick model showing the charge-charge interactions

between GABARAPL1 and ATG16L1 FIR. **e** The combined surface representation and the ribbon-stick model showing the hydrophobic interactions between GABARAPL1 and ATG16L1 FIR. In this drawing, ATG16L1 FIR is displayed in the ribbon-stick model, and GABARAPL1 is shown in surface representation, colored by different amino acid types. Specifically, the hydrophobic amino acid residues in the surface model of GABARAPL1 are drawn in yellow; the positively charged residues are drawn in blue; the negatively charged residues are drawn in red, and the uncharged polar residues are drawn in gray.

NAP1, NDP52, or TAX1BP1 consists of an acidic Asp followed by four consecutive hydrophobic residues, all of which participate in hydrophobic interactions with the relevant ATG8 family proteins<sup>26,31,42</sup>. Interestingly, unlike that of the unconventional AIM motifs of NAP1, NDP52, and TAX1BP1, the third residue of the core unconventional AIM motif of ATG16L1 is an acidic Glu residue (Supplementary Fig. 9b), which is directly involved in the interaction with GABARAPL1 (Fig. 3c). Therefore, ATG16L1 FIR represents a distinct type of unconventional AIM motif.

#### The relationships of FIP200, GABARAPL1, and WIPI2 in binding to ATG16L1

Based on our aforementioned structural analyses, ATG16L1 FIR adopts essentially the same key residues to recognize FIP200 Claw and GABARAPL1, such as the D239, I240, E241, and I243 residues (Figs. 2c and 3c and Supplementary Fig. 1). Thus, FIP200 and ATG8 family proteins should be mutually exclusive in binding to ATG16L1 FIR. As expected, further SEC coupled with SDS-PAGE assays confirmed that FIP200 Claw and GABARAPL1 are competitive in binding to ATG16L1 (Fig. 4a, b). Given that ATG16L1 FIR is C-terminally adjacent to the WBS1 of ATG16L1 (Fig. 1a), we also tested the relationship between WIPI2 and FIP200 or GABARAPL1 in binding to ATG16L1. Intriguingly,

we revealed that FIP200 Claw but not GABARAPL1 can form a stable ternary complex with WIPI2 and the ATG16L1(207–247) fragment that contains both WBS1 and FIR (Supplementary Fig. 14a), suggesting that WIPI2 and FIP200 can simultaneously bind to ATG16L1, consistent with a previous study<sup>11</sup>. In contrast, WIPI2 and ATG8 family proteins, such as GABARAPL1, are competitive in binding to ATG16L1(207–247) (Supplementary Fig. 14b), likely due to the potential steric hindrance.

#### The rational design of selective ATG16L1 mutant for binding to GABARAPL1 but not FIP200

Based on our previous study<sup>27</sup>, the consensus FIR motif ( $\Psi$ - $\Theta$ -X1-X2- $\Phi$ , where  $\Psi$  represents a phosphorylated Ser/Thr residue or an acidic Asp, Glu,  $\Theta$  represents a bulk hydrophobic Ile, Leu, Met or aromatic Phe, Tyr, Trp residue,  $\Phi$  represents a hydrophobic Leu, Ile or Val residue, and X1/X2 represents any residue), bears a striking resemblance to the sequence pattern of the core AIM sequence. Actually, the similarity between FIR and AIM severely interferes with our assessment of the individual contribution made by FIP200 and ATG8 family proteins when binding to ATG16L1 FIR. Therefore, it is necessary to develop selective ATG16L1 mutants that can exclusively interact with FIP200 or ATG8 family proteins. Based on our previous biochemical and structural characterizations of relevant FIR and AIM motifs<sup>27,43</sup>, we realized

**Table 2 | The measured binding affinities between ATG16L1 FIR and six mammalian ATG8 family proteins or their mutants by ITC-based binding assays**

ATG16L1	ATG8 protein	Kd (μM)
FIR	LC3A	7.28 ± 0.45
FIR	LC3B	18.10 ± 1.61
FIR	LC3C	6.27 ± 0.58
FIR	GABARAP	8.11 ± 0.48
FIR	GABARAPL1	4.59 ± 0.44
FIR	GABARAPL2	179.00 ± 41.50
FIR	GABARAPL1(I21Q)	11.40 ± 1.10
FIR	GABARAPL1(K48E)	N.D.
FIR	GABARAPL1(L50Q)	41.60 ± 9.01
FIR	GABARAPL1(R67E)	N.D.
FIR(D239R)	GABARAPL1	76.00 ± 75.30
FIR(I240Q)	GABARAPL1	85.20 ± 13.20
FIR(E241R)	GABARAPL1	56.30 ± 25.90
FIR(V242E)	GABARAPL1	10.50 ± 0.85
FIR(I243Q)	GABARAPL1	164.00 ± 140.00

that the first residue of the consensus core sequence of AIM, which is corresponding to the Ψ residue of FIR, can tolerate basic residues to some extent, such as Arg residue, while FIR cannot. In addition, the Θ residue of AIM prefers an aromatic Phe, Tyr, or Trp residue rather than a hydrophobic Ile, Leu, or Met residue. Eventually, we managed to devise a selective ATG16L1 D239R/I240F (DRIF) double mutant that can well recognize most ATG8 family proteins but not FIP200 (Fig. 4c–f and Supplementary Fig. 15). In addition, we also obtained a ATG16L1 I240Q/I243Q (IQIQ) double mutant, which essentially binds neither ATG8 family proteins nor FIP200 (Fig. 4c, d, g, h and Supplementary Fig. 15). Importantly, in agreement with our biochemical data (Fig. 4c–h and Supplementary Fig. 15), further overexpression-based co-immunoprecipitation assays showed that the DRIF mutant can selectively bind to GABARAPL1 but not FIP200 in cells (Fig. 5a, b). Concomitantly, the IQIQ mutation of ATG16L1 completely abolishes the specific interactions of ATG16L1 with FIP200 and GABARAPL1 in cells (Fig. 5a, b). Notably, in order to avoid potential ATG8ylation of ATG16L1 in cells<sup>44</sup>, the C-terminal Gly-Lys of GABARAPL1 was removed in these co-immunoprecipitation assays. Unfortunately, albeit with numerous attempts, we failed to obtain an ATG16L1 mutant, which can only bind to FIP200 but not GABARAPL1 with a comparable binding ability as the wild-type ATG16L1.

### The essential role of ATG16L1 FIR for the effective autophagic flux in canonical autophagy

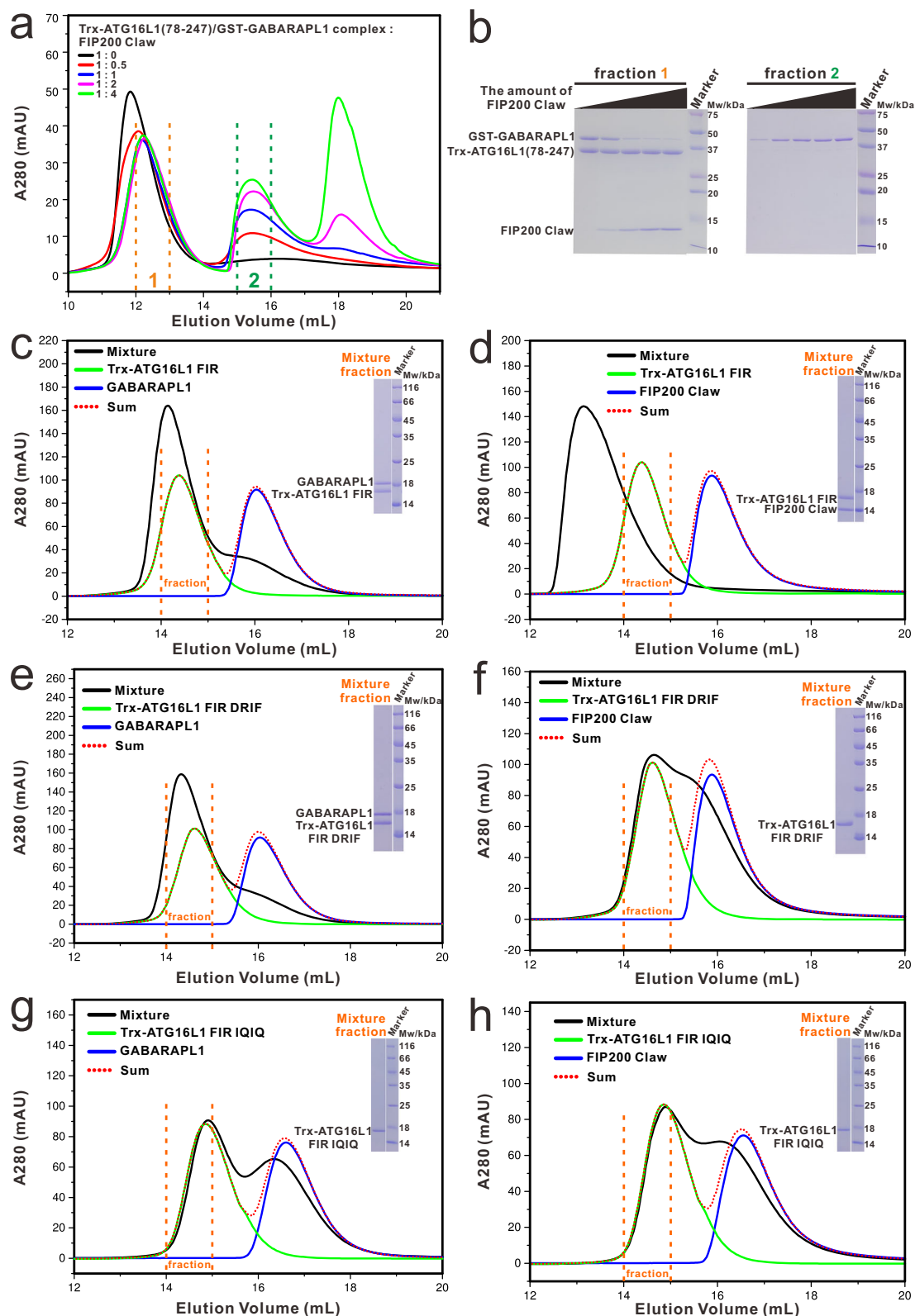
To further unravel the functional relevance of ATG16L1 FIR in autophagy, we back-transfected the *ATG16L1*-knockout HeLa cell line, which was generated in our previous study<sup>12</sup>, with relevant ATG16L1 plasmids to stably express the wild-type ATG16L1 or relevant ATG16L1 mutants, such as the DRIF mutant of ATG16L1 that only loses the FIP200-binding ability, or the ATG16L1 IQIQ mutant that simultaneously loses the abilities for interacting with FIP200 and ATG8 family proteins. In line with our previous study<sup>12</sup>, the autophagic flux in the *ATG16L1*-knockout cells was effectively rescued by the wild-type ATG16L1 (Fig. 5c–e). Meanwhile, starvation-induced lipidation of LC3B is unperturbed by the ATG16L1 DRIF or IQIQ mutation (Fig. 5c, e). However, both ATG16L1 DRIF and ATG16L1 IQIQ mutations significantly impair the autophagic degradation of p62 (Fig. 5c, d), underscoring an indispensable role of ATG16L1 FIR in starvation-induced autophagy. Notably, the DRIF mutation of ATG16L1 induces a much more severe impediment of the p62 degradation than the ATG16L1 IQIQ mutation (Fig. 5c, d), implying that the interaction of ATG16L1 FIR with FIP200 facilitates the

autophagy flux, whereas the interactions of ATG16L1 FIR with ATG8 family proteins attenuate the autophagy process. Taken together, these cell-based functional data clearly demonstrated that the interaction between ATG16L1 FIR and FIP200 is essential for the effective autophagic flux in canonical autophagy.

### Discussion

In this work, we uncovered that in addition to interacting with FIP200 Claw, ATG16L1 FIR can also serve as an unconventional AIM to recognize ATG8 family proteins. Furthermore, our biochemical and structural analyses revealed that ATG16L1 FIR can selectively bind to six mammalian ATG8 family proteins, but preferentially bind to GABARAPL1 and LC3C (Fig. 3a, f and Supplementary Fig. 6). Of note, detailed sequence alignment analysis elucidated that several key interface residues for interacting with ATG16L1 are quite different among six mammalian ATG8 family proteins (Supplementary Fig. 16). For instance, the residue corresponding to the R28 residue of GABARAPL1 that forms two hydrogen bonds with the backbone oxygen group of ATG16L1 I243, is a Lys residue in the LC3 subfamily; the residues corresponding to the bulk hydrophobic L55 and F60 residues in GABARAPL1 are two much smaller Val and Leu residues in LC3A and LC3B (Supplementary Fig. 16). The identification of these non-conserved interface residues among different ATG8 family proteins is likely to rationalize the selective recognition of different mammalian ATG8 orthologs by ATG16L1 FIR. Notably, based on this study together with previous reports<sup>27,31,42</sup>, the X1 position of FIR or AIM can accommodate acidic Glu residue as well as hydrophobic residues, including Ile, Val, and Cys (Fig. 1d), for engaging with FIP200 or ATG8 family proteins. It is noteworthy that the X1 residues in the FIR and/or AIM of SINTBAD and p62 are Ser/Thr residues that might undergo phosphorylation (Fig. 1d). Accordingly, whether there might be a potential regulatory role of X1 phosphorylation in tuning the interactions of SINTBAD, p62 or other related autophagic factors with FIP200 and ATG8 family proteins remains an open question that is worthwhile to be addressed in the future.

Based on our solid biochemical and structural results (Figs. 2 and 3), ATG16L1 FIR adopts many identical interface residues to interact with FIP200 Claw and ATG8 family proteins. Therefore, the simple deletion or mutagenesis of ATG16L1 used to disrupt the ATG16L1/FIP200 interaction in previous functional studies actually leads to the loss of the interactions of ATG16L1 with both FIP200 and ATG8 family proteins<sup>9–11,35</sup>. Consequently, the exact function of FIP200 for binding to ATG16L1 in autophagy remained unclear in previous studies. In this study, by developing and utilizing the ATG16L1 DRIF mutant that solely loses its ability to interact with FIP200 but not ATG8 family proteins, we confidently elucidated that the ATG16L1/FIP200 interaction is essential for the amino acid starvation-induced canonical autophagy. Notably, our relevant co-immunoprecipitation assays showed that the DRIF and IQIQ mutations completely disrupt the interaction of ATG16L1 with endogenous FIP200 but not ATG5 and GABARAP family proteins (Supplementary Fig. 17a–c), suggesting that in addition to the direct ATG16L1 FIR/ATG8 family protein interaction, ATG16L1 may indirectly associate with ATG8 family proteins through other adaptors, such as the ATG5-ATG12/ATG3 complex as reported in previous studies<sup>13,45,46</sup>. To avoid the potential influence of the indirect interaction of ATG16L1 with ATG8 family proteins through its ATG5BD region, we constructed relevant ATG16L1(78–607) variants, in which the ATG5BD region of ATG16L1 is removed. Subsequently, we conducted Co-IP assays to measure their interactions with endogenous GABARAP family proteins in the *ATG16L1*-knockout cell line. As anticipated, the Co-IP results showed that the wild-type ATG16L1(78–607) and the ATG16L1(78–607) DRIF mutant, but not the IQIQ mutant of ATG16L1(78–607), can readily interact with endogenous GABARAP family proteins (Supplementary Fig. 17d). Therefore, the ATG16L1 IQIQ mutant cannot directly interact with ATG8 family



proteins in cells. In all, given that the FIR/AIM motif is universally existed in many autophagy receptors<sup>27,28</sup>, the DRIF mutation strategy utilized for ATG16L1 in this study might also be employed to evaluate the respective roles of FIP200 and ATG8 family proteins in binding to relevant autophagy receptors during selective autophagy.

In addition to its crucial roles in canonical autophagy, previous functional studies well established that mammalian ATG16L1 specifically

senses pathogen invasion<sup>33,47</sup>, STING activation<sup>48</sup>, and lysosome damage<sup>49</sup> to conduct conjugation of ATG8 to single membranes (CASM) through its C-terminal WD40 repeats domain. Notably, the K490A mutation within the WD40 domain of ATG16L1 can specifically abolish CASM<sup>47</sup>. Intriguingly, the deficiency of FIP200 cannot block ATG16L1-mediated CASM process<sup>33,48</sup>. To ascertain whether ATG16L1 is involved in CASM, we utilized the *ATG16L1* KO cell line, and the *ATG16L1*

**Fig. 4 | Biochemical characterizations of the interactions of ATG16L1 variants with FIP200 Claw and GABARAPL1.** **a** Size-exclusion chromatography coupled with SDS-PAGE analysis of the Trx-ATG16L1(78–247)/GST-GABARAPL1 complex incubated with increasing molar ratio of FIP200 Claw proteins. **b** The SDS-PAGE combined with Coomassie-blue staining analyses of the protein components of the indicated “fraction 1” and “fraction 2” fractions collected from the analytical gel filtration chromatography experiment at different molar ratios of FIP200 Claw in (a). **c, d** Size-exclusion chromatography coupled with SDS-PAGE analysis of Trx-tagged ATG16L1 FIR wild-type with GABARAPL1 or FIP200 Claw. In this panel, “Sum” stands for the theoretical sum of Trx-tagged ATG16L1 FIR wild-type and GABARAPL1 or FIP200 Claw profiles, while “Mixture” stands for the Trx-tagged ATG16L1 FIR wild-type and GABARAPL1 or FIP200 Claw mixture sample. **e, f** Size-exclusion

chromatography coupled with SDS-PAGE analysis of Trx-tagged ATG16L1 FIR D239R/I240F mutant with GABARAPL1 or FIP200 Claw. In this panel, “Sum” stands for the theoretical sum of Trx-tagged ATG16L1 FIR D239R/I240F mutant and GABARAPL1 or FIP200 Claw profiles, while “Mixture” stands for the Trx-tagged ATG16L1 FIR D239R/I240F mutant and GABARAPL1 or FIP200 Claw mixture sample. **g, h** Size-exclusion chromatography coupled with SDS-PAGE analysis of Trx-tagged ATG16L1 FIR I240Q/I243Q mutant with GABARAPL1 or FIP200 Claw. In this panel, “Sum” stands for the theoretical sum of Trx-tagged ATG16L1 FIR I240Q/I243Q mutant and GABARAPL1 or FIP200 Claw profiles, while “Mixture” stands for the Trx-tagged ATG16L1 FIR I240Q/I243Q mutant and GABARAPL1 or FIP200 Claw mixture sample.

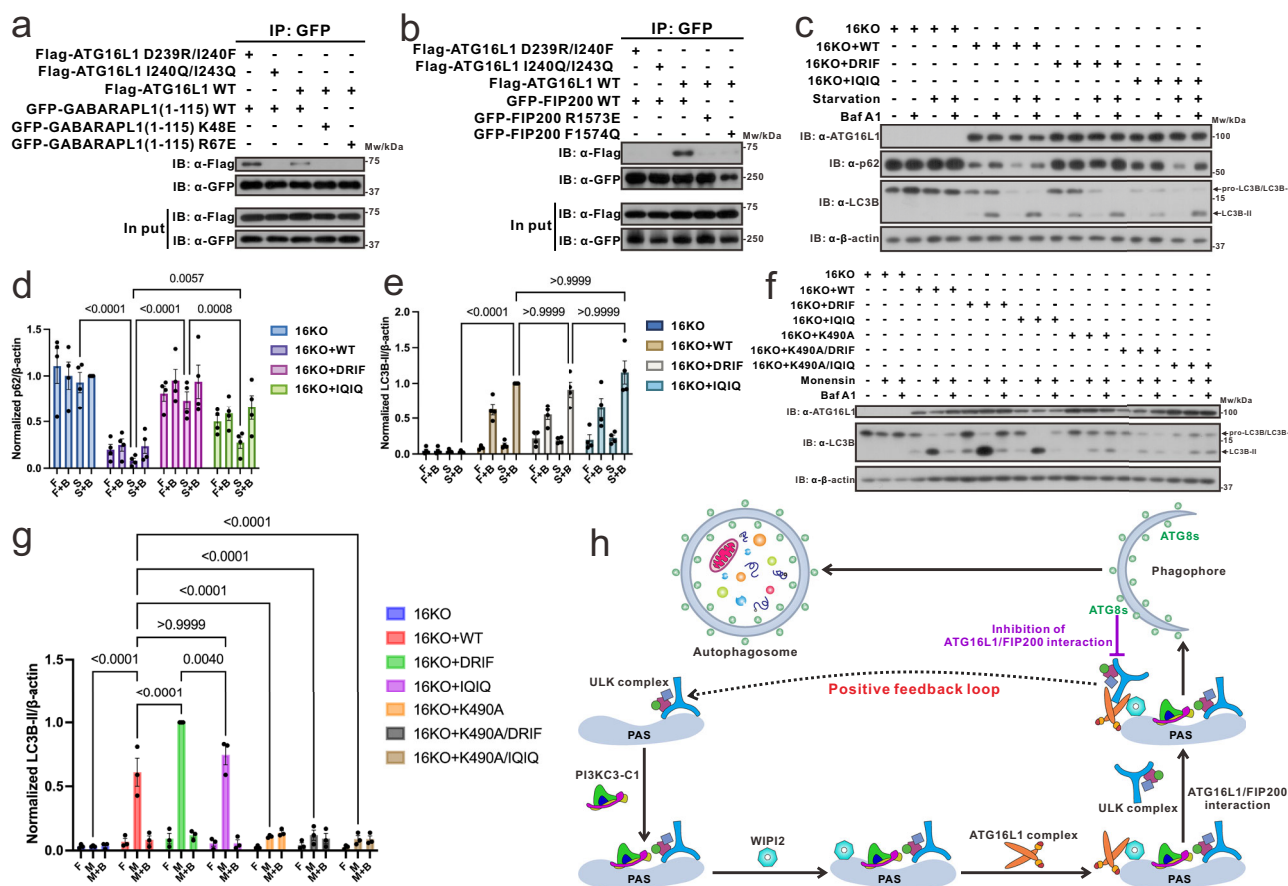


**Fig. 5 | Cell-based assays of the interactions of ATG16L1 with GABARAPL1 and FIP200 in autophagy.** **a** Co-immunoprecipitation assays showing that point mutations of key interface residues of GABARAPL1 observed in the GABARAPL1/ATG16L1 FIR complex structure essentially disrupt their specific interaction in cells. “IB” means immunoblotting. **b** Co-immunoprecipitation assays showing that point mutations of both devised ATG16L1 mutant and key interface residues of FIP200 observed in the FIP200 Claw/ATG16L1 FIR complex structure decrease or essentially disrupt the specific interaction between FIP200 and ATG16L1 in cells. **c** Western blot-based measurements of the LC3B lipidation and p62 degradation levels in *ATG16L1*-knockout HeLa cells (16KO) as well as that rescued with mEGFP-tagged WT ATG16L1 (16KO + WT), ATG16L1 D239R/I240F mutant (16KO + DRIF), or ATG16L1 I240Q/I243Q mutant (16KO + IQIQ) treated for 4 h using D10 + PS normal medium (F), D10 + PS normal medium treated with bafilomycin A1 at 400 nM (F + B), amino acid starvation medium (S), or amino acid starvation medium treated with bafilomycin A1 at 400 nM (S + B). **d** The levels of p62 and β-actin in (c) were quantified in ImageJ and normalized to that of 16KO cells treated with S + B. The data is presented as means ± SEM from four independent experiments. **e** The levels of LC3B-II and β-actin in (c) were quantified in ImageJ and normalized to the

16KO + WT cells treated with S + B. The data is presented as means ± SEM from four independent experiments. **f** Western blot-based measurements of the LC3B lipidation in *ATG16L1*-knockout HeLa cells (16KO) as well as that rescued with mEGFP-tagged WT ATG16L1 (16KO + WT), ATG16L1 D239R/I240F mutant (16KO + DRIF), ATG16L1 I240Q/I243Q mutant (16KO + IQIQ), ATG16L1 K490A mutant (16KO + K490A), ATG16L1 K490A/D239R/I240F mutant (16KO + K490A/DRIF), or ATG16L1 K490A/I240Q/I243Q mutant (16KO + K490A/IQIQ) treated for 1 h using D10 + PS normal medium (F), D10 + PS normal medium treated with monensin at 100 μM (M), or D10 + PS normal medium treated with monensin at 100 μM and bafilomycin A1 at 400 nM (M + B). **g** The levels of LC3B-II and β-actin in (f) were quantified and normalized to that of 16KO + DRIF cells treated with monensin at 100 μM (M). The data is presented as means ± SEM from three independent experiments. Statistical analyses were all performed in GraphPad Prism 9 by two-way analysis of variance (ANOVA) followed by Bonferroni multiple comparisons test, and P value style is P = 0.1234 [not significant (ns)], \*P = 0.0332, \*\*P = 0.0021, \*\*\*P = 0.0002, and \*\*\*\*P < 0.0001. **h** A proposed model depicting the functions of the FIP200/ATG16L1 and ATG8s/ATG16L1 interactions in canonical autophagy.

KO cell lines reconstituted with the wild-type ATG16L1 or relevant ATG16L1 variant, including the ATG16L1 DRIF mutant, IQIQ mutant, K490A mutant, K490A/D239R/I240F mutant (K490A/DRIF), or K490A/I240Q/I243Q mutant (K490A/IQIQ), and measured the ionophore monensin-induced CASM levels in these cells. As expected, the knockout of *ATG16L1* and the K490A mutation of *ATG16L1* essentially abolish or significantly attenuate the monensin-induced CASM (Fig. 5f, g). Interestingly, the ATG16L1 DRIF mutant significantly promotes the monensin-induced LC3B lipidation compared with the wild-type ATG16L1 and the ATG16L1 IQIQ mutant (Fig. 5f, g). Moreover, our co-immunoprecipitation assays showed that the monensin treatment considerably impairs the interaction of ATG16L1 with endogenous FIP200 but not ATG5, WIPI2, and GABARAP family proteins (Supplementary Fig. 18). Taken together, based on these observations, we concluded that the interaction of ATG16L1 with FIP200 impedes CASM, while the interaction of ATG16L1 with ATG8 family protein promotes the CASM process.

Notably, p62-ubiquitin condensates recruit the ULK complex upon the interaction between p62 FIR and FIP200 Claw, thereby promoting the autophagy-dependent degradation of ubiquitinated cargoes<sup>28</sup>. In this study, our biochemical and structural data demonstrated that ATG16L1 FIR is directly involved in the interaction with FIP200 Claw (Figs. 1e, 2 and 4d). Thus, the deletion of FIP200 Claw not only abolishes the association between p62 and FIP200, but also eliminates the interaction of FIP200 with ATG16L1 as well as many other autophagy receptors, such as TAX1BP1, that can indirectly associate with p62 through NBR1<sup>50</sup>. Therefore, the related functional data derived from the deprivation of FIP200 Claw in the previous study should be interpreted with caution<sup>28</sup>.

In mammals, ATG16L1 is equipped with two distinct WIPI2-binding sites and one FIP200-interacting region to facilitate the normal progression of autophagy<sup>9,10,12</sup>. In contrast, ATG16 in yeast encompasses only one conserved site to bind ATG21, the yeast homolog of WIPI2<sup>51,52</sup>. In addition, the direct interaction between the ATG1 complex and the ATG16 complex is mediated by the N-terminal segment of yeast ATG12 rather than mammalian ATG16L1 FIR<sup>53</sup>. Thus, although the detailed binding mechanisms are different, the associations of the ATG16/ATG16L1 complex with the ATG1/ULK complex and ATG21/WIPI2 in canonical autophagy are well-conserved from yeast to mammals. Based on our functional data in this study, the ATG16L1 FIR/FIP200 interaction is essential for starvation-induced canonical autophagy (Fig. 5c–e). Therefore, the expeditious autophagosome biogenesis in canonical autophagy is unlikely to be adequately explained by merely two distinct linear hierarchical pathways started from the ULK complex. Accordingly, we proposed a positive feedback loop model to illustrate the function of ATG16L1 in canonical autophagy. In this model, the FIP200-containing ULK complex at PAS initiates the translocation of the PI3KC3-C1 complex (Fig. 5h). Subsequently, the activated PI3KC3-C1 complex results in the redistribution of WIPI2 through the generation of substantial PI3P molecules (Fig. 5h). Whereafter, WIPI2 recruits and activates the ATG16L1 complex, which inversely promotes the recruitment of additional ULK complexes to PAS through a binding mechanism between ATG16L1 FIR and FIP200 Claw as uncovered in this study, thereby generating a positive feedback loop to facilitate the rapid expansion of phagophore membrane to form autophagosome (Fig. 5h). As this autophagic process continues, the abundant lipidated ATG8 family proteins generated by the ATG16L1 complex on phagophore membrane can in turn compete with FIP200 for binding to ATG16L1, thereby attenuating this positive feedback loop to prevent the excessive activation of autophagy (Fig. 5h).

## Methods

### Materials

HEK293T and HeLa cell lines were kindly provided by Prof. Junying Yuan from Interdisciplinary Research Center on Biology and

Chemistry, CAS, Shanghai, China. All cell lines were cultivated with Dulbecco's modified Eagle's medium (Sigma-Aldrich) supplemented with 10% fetal bovine serum (Sigma-Aldrich) and 1% penicillin-streptomycin (Thermo Fisher Scientific) (hereafter referred to as D10 + PS) at 37 °C in humidified 5% CO<sub>2</sub> atmosphere. The full-length human *WIPI2b*, *ATG8s*, *ATG16L1*, and *FIP200* genes were obtained from Prof. Jiahui Han from School of Life Sciences, Xiamen University, Xiamen, China. The synthetic peptide "EQDDDEIVDET" (ATG16L1 FIR) was purchased from the China Peptides company, and the purity of the commercially synthesized peptides was >98%.

### Protein expression and purification

The DNA fragments encoding human FIP200 (residues 1490–1594) and WIPI2b (residues 13–362 without 265–297) were cloned into pET-SUMO-3C vector or pET-32M-3C vector (modified versions of pET-32a vector containing an N-terminal SUMO or Trx tag). The DNA fragments encoding ATG16L1 (residues 207–247, 78–235, 235–247, and 78–247) were all cloned into pACYC-Trx1-3C vector (a modified version of pACYC vector containing an N-terminal Trx tag) or pET-GST-3C vector (a modified version of pET-32a vector containing an N-terminal GST tag). Meanwhile, the DNA fragments encoding six human ATG8 family proteins were all cloned into pET-32M-3C vector or pET-GST-3C vector. Of note, 6xHis was placed on either the N-terminal or the C-terminal of target proteins. For co-immunoprecipitation assays, the DNA fragments encoding human GABARAPL1(1–115) and full-length FIP200 were separately cloned into pEGFP-C1 vector and pmEGFP-C1 vector (a modified version of pEGFP-C1 with an A206K mutation that monomerizes EGFP), as well as full-length ATG16L1 into pFlag-CMV-2 vector. All point mutations of WIPI2b, FIP200, GABARAPL1, and ATG16L1 used in this study were generated through standard PCR-based mutagenesis method and further confirmed by DNA sequencing.

Recombinant proteins were all expressed in BL21 (DE3) *E. coli* cells induced by 200 μM IPTG overnight at 16 °C. The bacterial cell pellets were re-suspended in the binding buffer (50 mM Tris, 500 mM NaCl, and 5 mM imidazole at pH 7.9), and then lysed by the ultrahigh-pressure homogenizer FB-110XNANO homogenizer machine (Shanghai Litu Machinery Equipment Engineering Co., Ltd.). Then, the lysate was spun down by centrifuge at 35,000 × *g* for 35 min to remove the pellets fractions. All proteins were purified by Ni<sup>2+</sup>-NTA agarose (GE Healthcare) affinity chromatography and further purified by size-exclusion chromatography (Superdex 75 or 200 26/60 column; GE Healthcare) equilibrated with the column buffer containing 20 mM Tris, 100 mM NaCl, 1 mM DTT, and 1 mM EDTA at pH 7.5. To obtain the FIP200 Claw/ATG16L1 FIR complex used for crystallization, the FIP200/ATG16L1 complex was obtained through the co-expression of Trx-FIP200(1490–1594) and Trx-ATG16L1(235–247). The N-terminal Trx tags of relevant FIP200 and ATG16L1 proteins were cleaved by 3C protease and further removed by HisTrap excel column (GE Healthcare). Finally, the FIP200 Claw/ATG16L1 FIR complex and the GABARAPL1/ATG16L1 FIR complex were further purified through Superdex 75 column equilibrated with the aforementioned column buffer. Specifically, for six human ATG8 family proteins, their Trx tags were removed by MonoQ 10/10 ion-exchange column (GE Healthcare). Meanwhile, uniformly <sup>15</sup>N-labeled GABARAPL1 proteins were prepared by growing bacteria in M9 minimal medium using <sup>15</sup>NH<sub>4</sub>Cl (Cambridge Isotope Laboratories Inc.) as the sole nitrogen source.

### ITC assay

ITC measurements were all carried out on a MicroCal PEAQ-ITC (Malvern) calorimeter at 25 °C. All protein samples were prepared in the same buffer containing 20 mM Tris, 100 mM NaCl, 1 mM DTT at pH 7.5. For each ITC experiment in this study, the concentrated (~50 μM) proteins were loaded into the cell, and the other titrated proteins (~500 μM) were loaded into the syringe. The titration processes were performed by injecting proteins from syringe into the

cell at time intervals of 2 min to ensure that the titration peak returned to the baseline. The titration data were analyzed using the Malvern MicroCal PEAQ-ITC analysis program and fitted using the one-site binding model.

### Size-exclusion chromatography

Size-exclusion chromatography was carried out on an AKTA FPLC system (GE Healthcare). Purified proteins were loaded onto a Superdex 200 or 75 increase 10/300 GL column (GE Healthcare) equilibrated with the same column buffer. The fitting results were further output to the Origin 9 software and aligned with each other.

### NMR spectroscopy

The  $^{15}\text{N}$ -labeled protein samples for NMR titration experiments were concentrated to ~0.1 mM. All the protein samples for NMR studies were prepared in the 50 mM potassium phosphate buffer containing 100 mM NaCl, 1 mM DTT, and 10%  $\text{D}_2\text{O}$  at pH 6.5. All NMR experiments were conducted at 25 °C on an Agilent 800 MHz spectrometer equipped with an actively z gradient shielded triple resonance probe at the Shanghai Institute of Organic Chemistry. NMR data were acquired using Agilent Vnmrj 3.2. The pulse sequence used for the  $^1\text{H}$ - $^{15}\text{N}$  HSQC experiment in this study is an HSQC gradient sensitivity enhanced version for N15 with options for TROSY on N15/H1 and for T1, T1rho, and T2 relaxation measurements of the N15 nuclei<sup>54,55</sup>. The spectral widths of each  $^1\text{H}$ - $^{15}\text{N}$  HSQC experiment conducted in this study were set to 11,160.714 Hz (x-axis, 14 ppm) and 2917.432 Hz (y-axis, 36 ppm), and the number of scans was set to 32. Meanwhile, the acquisition time for each  $^1\text{H}$ - $^{15}\text{N}$  HSQC spectrum is roughly 155 min. All NMR spectra were processed using NMRDraw 8.1<sup>56</sup>, and analyzed using Sparky 3.115 (<https://www.cgl.ucsf.edu/home/sparky/>) or the CCPN software<sup>57</sup>. Specifically, the assignment of the NMR peaks in the  $^1\text{H}$ - $^{15}\text{N}$  HSQC spectrum of the  $^{15}\text{N}$ -labeled GABARAPL1 in this study was accomplished using the CCPN software based on the previously reported backbone assignment of GABARAPL1 (BMRB Entry 17412)<sup>41</sup>.

### Multi-angle light scattering

For multi-angle light-scattering measurement, the purified FIP200 (1490–1594)/ATG16L1(78–247) complex sample was injected into an AKTA FPLC system (GE Healthcare) with a Superdex 200 increase 10/300 GL column (GE Healthcare) with the same column buffer mentioned before. The chromatography system was coupled to a static light-scattering detector (miniDawn, Wyatt Technology) and a differential refractive index detector (Optilab, Wyatt Technology). Data were collected every 0.5 s with a flow rate of 0.5 mL/min. Data were analyzed using the ASTRA 6 software (Wyatt Technology) and drawn using the Origin 9 software.

### Fluorescence polarization assay

Fluorescence anisotropy binding assays were performed on the SpectraMax i3x Multi-Mode Detection Platform from Molecular Devices, using a 485 nm excitation filter and a 535 nm emission filter. Peptides were labeled with fluorescein isothiocyanate isomer I (FITC, Sigma-Aldrich) at their N-terminal  $\text{NH}_2$ . In this assay, the FITC-labeled peptide (~0.3  $\mu\text{M}$ ) was titrated with increasing amount of testing proteins in the column buffer at 25 °C. The  $K_d$  values were obtained by fitting the titration curves with the classical one-site binding model using GraphPad Prism 9 software.

### Protein crystallization and structural elucidation

Crystals of the FIP200(1490–1594)/ATG16L1(235–247) complex and the GABARAPL1/ATG16L1(235–247) complex were both obtained using the sitting-drop vapor-diffusion method at 16 °C. The crystal-growing condition of the FIP200(1490–1594)/ATG16L1(235–247) complex (38 mg/mL) contains 10% v/v 2-Propanol, 0.1 M BICINE (pH 8.5), and 30% w/v Polyethylene glycol 1500. As for the GABARAPL1/

ATG16L1(235–247) complex, the purified GABARAPL1 protein (27 mg/mL) was saturated with the ATG16L1 FIR peptide with a molar ratio up to 1:10. Crystals were observed in the condition containing 0.1 M Sodium cacodylate (pH 6.5), 40% v/v MPD, and 5% w/v PEG 8000. Before diffraction experiments, relevant amount of glycerol was added as the cryo-protectant. A 1.61 Å resolution X-ray data set for the FIP200(1490–1594)/ATG16L1(235–247) complex and a 1.76 Å resolution X-ray data set for the GABARAPL1/ATG16L1(235–247) complex were collected at the beamline BL19U1, BL02U1, and BL10U2 of the Shanghai Synchrotron Radiation Facility<sup>58</sup>. The diffraction data were processed using autoPROC<sup>59</sup>. The phase problems of the FIP200/ATG16L1 complex and the GABARAPL1/ATG16L1 complex were all solved by molecular replacement method by using the FIP200 Claw structure (PDB ID: 6DCE) and the GABARAPL1 structure (PDB ID: 5LXI), respectively, as the search model with PHASER<sup>60</sup>. The initial structural models were rebuilt manually using COOT<sup>61</sup>, and then refined through PHENIX<sup>62</sup>. Further manual model building and adjustments were completed via COOT<sup>61</sup>. The qualities of the final models were validated by MolProbity<sup>63</sup>. The final refinement statistics of solved structures in this study are listed in Supplementary Table 1. All the structural diagrams were prepared using the program PyMOL (<http://www.pymol.org/>).

### GST pull-down assay

Purified GST-tagged ATG16L1 FIR (wild-type or mutants) and FIP200 Claw or ATG8 family proteins were applied to Glutathione beads (Smart-Lifesciences) and incubated for 60 min at 4 °C. The beads and non-bound proteins were separated by centrifugation at 800 g for 3 min at 4 °C. After washing several times with the cold wash buffer (50 mM Tris, 150 mM NaCl, and 0.1% NP-40 at pH 7.5), the beads were re-suspended with the SDS-PAGE sample buffer and boiled at 65 °C for 10 min. The prepared samples were further analyzed by SDS-PAGE.

### Co-immunoprecipitation assay

Flag-tagged ATG16L1 plasmids (wild-type or mutants) were co-transfected into HEK293T cells using Lipofectamine 2000 transfection reagent (Thermo Fisher Scientific) or Lipofectamine 6000 transfection reagent (Beyotime) with mEGFP-tagged FIP200 or EGFP-tagged GABARAPL1(I-115) plasmids. Cells were collected 24 h after transfection and lysed in an ice-cold cell lysis buffer (50 mM Tris, 150 mM NaCl, 0.5% NP-40, 1 mM PMSF, 1% protease inhibitor cocktail at pH 7.5) for 20–40 min at 4 °C. Lysates were centrifuged at 14,500 × g for 15 min at 4 °C to separate soluble fractions and cell debris. Supernatants were applied to anti-GFP mAb-Agarose (Medical & Biological Laboratories) and incubated for 40–60 min at 4 °C. The beads and non-bound proteins were separated by centrifugation at 800 × g for 3 min at 4 °C. After washing several times with the cold wash buffer (50 mM Tris, 150 mM NaCl, and 0.1% or 0.5% NP-40 at pH 7.5), the beads were re-suspended with the SDS-PAGE sample buffer and boiled at 65 °C for 10 min. The prepared samples were analyzed by SDS-PAGE. The EGFP-tagged GABARAPL1(I-115), mEGFP-tagged FIP200, and Flag-tagged ATG16L1 were detected by western blot using the anti-GFP (Proteintech, 50430-2-AP, 1:1000 dilution), anti-GFP (Proteintech, 66002-1-Ig, 1:2000 dilution), anti-Flag (Proteintech, 20543-1-AP, 1:1000 dilution), and anti-Flag (Proteintech, 66008-4-Ig, 1:2000 dilution) primary antibodies.

Specifically, for co-immunoprecipitation assays to detect the interactions of ATG16L1 with relevant endogenous proteins, rescued HeLa cells were harvested 24 h after seeding. Endogenous FIP200, ATG5-ATG12, WIPI2, GABARAP family proteins, and mEGFP-tagged wild-type ATG16L1 or relevant ATG16L1 mutants were detected by western blot using the anti-FIP200 (Proteintech, 17250-1-AP, 1:2000 dilution), anti-ATG5 (Proteintech, 81803-1-RR, 1:2000 dilution), anti-WIPI2 (Proteintech, 28820-1-AP, 1:2000 dilution), anti-GABARAP family (Selleck, F1156, 1:2000 dilution), and anti-GFP (Abmart, M20004M, 1:2000 dilution) primary antibodies.

### Generation of relevant ATG16L1 stable cell lines

The mEGFP-tagged wild-type ATG16L1 or relevant ATG16L1 mutant was cloned into the pMSCV-blasticidin vector, and subsequently was co-transfected into HEK293T cells with VSV.G and gag/pol using Lipofectamine 6000 transfection reagent (Beyotime). The virus-containing medium was filtered through a 0.45- $\mu$ m-pore syringe filter and concentrated by using lentivirus concentration reagent (Biodragon). Notably, the sgRNA-targeting region of ATG16L1 at pMSCV-blasticidin vector was synonymously mutated to avoid being targeted again by the Cas9 enzyme. Finally, *ATG16L1*-knockout cells were incubated with polybrene (Sigma-Aldrich) and concentrated virus, and treated with blasticidin (7.5  $\mu$ g/mL; InvivoGen) to generate stable polyclonal cell lines.

### Autophagy induction

The *ATG16L1*-knockout HeLa cells, which were generated in our previous study<sup>12</sup>, were rescued by lentiviral transduction with mEGFP-tagged wild-type ATG16L1 (16KO + WT), ATG16L1 D239R/I240F mutant (16KO + DRIF), or ATG16L1 I240Q/I243Q mutant (16KO + IQIQ). The *ATG16L1*-knockout HeLa cells and rescued cells were separately seeded on a six-well plate. The following day, cells were incubated for 4 h with D10 + PS, D10 + PS with bafilomycin A1 (Selleck) at 400 nM, amino acid starvation medium (BOSTER), and amino acid starvation medium with bafilomycin A1 at 400 nM. After starvation treatment, cells were re-suspended with the SDS-PAGE sample buffer and boiled for 10 min at 100 °C. The samples were detected by western blot using specific ATG16L1 antibody (1:2000; Abcam, catalog no. ab187671), LC3B antibody (1:2000; Abcam, catalog no. ab192890),  $\beta$ -actin antibody (1:5000; Proteintech, catalog no. 66009-1-Ig), and p62 antibody (1:2000; Cell Signaling Technology, catalog no. 39749S). The data are presented as means  $\pm$  SEM from four independent experiments. Statistical analyses were performed in GraphPad Prism 9 by two-way analysis of variance (ANOVA) followed by Bonferroni multiple comparisons test, and P value style is P = 0.1234 (not significant (ns)), \*P = 0.0332, \*\*P = 0.0021, \*\*\*P = 0.0002, and \*\*\*\*P < 0.0001.

### CASM induction

The *ATG16L1*-knockout HeLa cells were rescued by lentiviral transduction with mEGFP-tagged wild-type ATG16L1 (16KO + WT), ATG16L1 D239R/I240F mutant (16KO + DRIF), ATG16L1 I240Q/I243Q mutant (16KO + IQIQ), ATG16L1 K490A mutant (16KO + K490A), ATG16L1 K490A/D239R/I240F mutant (16KO + K490A/DRIF), or ATG16L1 K490A/I240Q/I243Q mutant (16KO + K490A/IQIQ). The *ATG16L1*-knockout HeLa cells and rescued cells were separately seeded on a six-well plate. The following day, cells were incubated for 1 h with D10 + PS, D10 + PS with monensin (Selleck) at 100  $\mu$ M, D10 + PS with monensin at 100  $\mu$ M, and bafilomycin A1 (Selleck) at 400 nM. After treatment, cells were re-suspended with the SDS-PAGE sample buffer and boiled for 10 min at 100 °C. The samples were detected by western blot using specific ATG16L1 antibody (1:2000; Abcam, catalog no. ab187671), LC3B antibody (1:2000; Abcam, catalog no. ab192890), and  $\beta$ -actin antibody (1:5000; Proteintech, catalog no. 66009-1-Ig). The data are presented as means  $\pm$  SEM from three independent experiments. Statistical analyses were performed in GraphPad Prism 9 by two-way analysis of variance (ANOVA) followed by Bonferroni multiple comparisons test, and P value style is P = 0.1234 (not significant (ns)), \*P = 0.0332, \*\*P = 0.0021, \*\*\*P = 0.0002, and \*\*\*\*P < 0.0001.

### Statistics and reproducibility

All the size-exclusion chromatography-based experiments, multi-angle light-scattering experiments, SDS-PAGE combined with Coomassie-blue staining experiments, fluorescence polarization (FP)-based experiments, ITC experiments, and NMR-based experiments in this study were independently repeated once with similar results.

Meanwhile, all co-immunoprecipitation experiments in this study were independently repeated twice with similar results.

### Reporting summary

Further information on research design is available in the Nature Portfolio Reporting Summary linked to this article.

### Data availability

The coordinates and structure factors of the FIP200 Claw/ATG16L1 FIR complex and the GABARAPL1/ATG16L1 FIR complex solved in this study have been deposited in the Protein Data Bank under the accession codes 9J54 and 9JF2, respectively. The backbone assignment data of GABARAPL1 used in this study are available in the BMRB database under accession number 17412. PDB codes of previously published structures used in this study are 6DCE and 5LXI. Source data are provided as a Source data file. All additional experimental data are available from the corresponding author on request. Source data are provided with this paper.

### References

- Lamb, C. A., Yoshimori, T. & Tooze, S. A. The autophagosome: origins unknown, biogenesis complex. *Nat. Rev. Mol. Cell Biol.* **14**, 759–774 (2013).
- Levine, B. & Kroemer, G. Biological functions of autophagy genes: a disease perspective. *Cell* **176**, 11–42 (2019).
- Yamamoto, H., Zhang, S. & Mizushima, N. Autophagy genes in biology and disease. *Nat. Rev. Genet.* **24**, 382–400 (2023).
- Dikic, I. & Elazar, Z. Mechanism and medical implications of mammalian autophagy. *Nat. Rev. Mol. Cell Biol.* **19**, 349–364 (2018).
- Feng, Y. C., He, D., Yao, Z. Y. & Klionsky, D. J. The machinery of macroautophagy. *Cell Res.* **24**, 24–41 (2014).
- Hurley, J. H. & Young, L. N. Mechanisms of autophagy initiation. *Annu. Rev. Biochem.* **86**, 225–244 (2017).
- Zheng, Q. et al. Calcium transients on the ER surface trigger liquid-liquid phase separation of FIP200 to specify autophagosome initiation sites. *Cell* **185**, 4082–4098 e22 (2022).
- Matsunaga, K. et al. Autophagy requires endoplasmic reticulum targeting of the PI3-kinase complex via Atg14L. *J. Cell Biol.* **190**, 511–521 (2010).
- Gammoh, N., Florey, O., Overholtzer, M. & Jiang, X. Interaction between FIP200 and ATG16L1 distinguishes ULK1 complex-dependent and -independent autophagy. *Nat. Struct. Mol. Biol.* **20**, 144–149 (2013).
- Nishimura, T. et al. FIP200 regulates targeting of Atg16L1 to the isolation membrane. *EMBO Rep.* **14**, 284–291 (2013).
- Dooley, H. C. et al. WIPI2 links LC3 conjugation with PI3P, autophagosome formation, and pathogen clearance by recruiting Atg12-5-16L1. *Mol. Cell* **55**, 238–252 (2014).
- Gong, X. et al. ATG16L1 adopts a dual-binding site mode to interact with WIPI2b in autophagy. *Sci. Adv.* **9**, eadf0824 (2023).
- Otomo, C., Metlagel, Z., Takaesu, G. & Otomo, T. Structure of the human ATG12-ATG5 conjugate required for LC3 lipidation in autophagy. *Nat. Struct. Mol. Biol.* **20**, 59–66 (2013).
- Fujita, N. et al. The Atg16L complex specifies the site of LC3 lipidation for membrane biogenesis in autophagy. *Mol. Biol. Cell* **19**, 2092–2100 (2008).
- Bozic, M. et al. A conserved ATG2-GABARAP family interaction is critical for phagophore formation. *EMBO Rep.* **21**, e48412 (2020).
- Strong, L. M. et al. Structural basis for membrane recruitment of ATG16L1 by WIPI2 in autophagy. *eLife* **10**, e70372 (2021).
- Gatica, D., Lahiri, V. & Klionsky, D. J. Cargo recognition and degradation by selective autophagy. *Nat. Cell Biol.* **20**, 233–242 (2018).
- Stolz, A., Ernst, A. & Dikic, I. Cargo recognition and trafficking in selective autophagy. *Nat. Cell Biol.* **16**, 495–501 (2014).

19. Johansen, T. & Lamark, T. Selective autophagy mediated by autophagic adapter proteins. *Autophagy* **7**, 279–296 (2011).
20. Rogov, V., Dotsch, V., Johansen, T. & Kirkin, V. Interactions between autophagy receptors and ubiquitin-like proteins form the molecular basis for selective autophagy. *Mol. Cell* **53**, 167–178 (2014).
21. Green, D. R. & Levine, B. To be or not to be? How selective autophagy and cell death govern cell fate. *Cell* **157**, 65–75 (2014).
22. Kirkin, V. History of the selective autophagy research: How did it begin and where does it stand today?. *J. Mol. Biol.* **432**, 3–27 (2020).
23. Farre, J. C. & Subramani, S. Mechanistic insights into selective autophagy pathways: lessons from yeast. *Nat. Rev. Mol. Cell Biol.* **17**, 537–552 (2016).
24. Kirkin, V. & Rogov, V. V. A diversity of selective autophagy receptors determines the specificity of the autophagy pathway. *Mol. Cell* **76**, 268–285 (2019).
25. Johansen, T. & Lamark, T. Selective autophagy: ATG8 family proteins, LIR motifs and cargo receptors. *J. Mol. Biol.* **432**, 80–103 (2020).
26. Zhang, M. F. et al. Mechanistic insights into the interactions of TAX1BP1 with RB1CC1 and mammalian ATG8 family proteins. *Proc. Natl. Acad. Sci. USA* **121**, e2315550121 (2024).
27. Zhou, Z. et al. Phosphorylation regulates the binding of autophagy receptors to FIP200 Claw domain for selective autophagy initiation. *Nat. Commun.* **12**, 1570 (2021).
28. Turco, E. et al. FIP200 Claw domain binding to p62 promotes autophagosome formation at ubiquitin condensates. *Mol. Cell* **74**, 330 (2019).
29. Vargas, J. N. S. et al. Spatiotemporal control of ULK1 activation by NDP52 and TBK1 during selective autophagy. *Mol. Cell* **74**, 347 (2019).
30. Smith, M. D. et al. CCPG1 is a non-canonical autophagy cargo receptor essential for ER-phagy and pancreatic ER proteostasis. *Dev. Cell* **44**, 217 (2018).
31. Fu, T. et al. Structural and biochemical advances on the recruitment of the autophagy-initiating ULK and TBK1 complexes by autophagy receptor NDP52. *Sci. Adv.* **7**, eabi6582 (2021).
32. Sorbara, M. T. et al. Complement C3 drives autophagy-dependent restriction of cyto-invasive bacteria. *Cell Host Microbe* **23**, 644–652 e5 (2018).
33. Xu, Y. et al. A bacterial effector reveals the V-ATPase-ATG16L1 axis that initiates xenophagy. *Cell* **178**, 552–566 e20 (2019).
34. Gammoh, N. The multifaceted functions of ATG16L1 in autophagy and related processes. *J. Cell Sci.* **133**, jcs249227 (2020).
35. Fujita, N. et al. Recruitment of the autophagic machinery to endosomes during infection is mediated by ubiquitin. *J. Cell Biol.* **203**, 115–128 (2013).
36. Behrends, C., Sowa, M. E., Gygi, S. P. & Harper, J. W. Network organization of the human autophagy system. *Nature* **466**, 68–76 (2010).
37. Le Guerroue, F. et al. TNIP1 inhibits selective autophagy via bipartite interaction with LC3/GABARAP and TAX1BP1. *Mol. Cell* **83**, 927–941 e8 (2023).
38. Wu, S. et al. Structural basis for TNIP1 binding to FIP200 during mitophagy. *J. Biol. Chem.* **300**, 107605 (2024).
39. Ravenhill, B. J. et al. The cargo receptor NDP52 initiates selective autophagy by recruiting the ULK complex to cytosol-invading bacteria. *Mol. Cell* **74**, 320 (2019).
40. North, B. J., Ohnstad, A. E., Ragusa, M. J. & Shoemaker, C. J. The LC3-interacting region of NBR1 is a protein interaction hub enabling optimal flux. *J. Cell Biol.* **224**, e202407105 (2025).
41. Rozenknop, A. et al. Characterization of the interaction of GABARAPL-1 with the LIR motif of NBR1. *J. Mol. Biol.* **410**, 477–487 (2011).
42. von Muhlinen, N. et al. LC3C, bound selectively by a noncanonical LIR motif in NDP52, is required for antibacterial autophagy. *Mol. Cell* **48**, 329–342 (2012).
43. Cheng, X. F. et al. Structural basis of FYCO1 and MAP1LC3A interaction reveals a novel binding mode for Atg8-family proteins. *Autophagy* **12**, 1330–1339 (2016).
44. Nguyen, T. N. et al. ATG4 family proteins drive phagophore growth independently of the LC3/GABARAP lipidation system. *Mol. Cell* **81**, 2013–2030 e9 (2021).
45. Metlagel, Z., Otomo, C., Takaesu, G. & Otomo, T. Structural basis of ATG3 recognition by the autophagic ubiquitin-like protein ATG12. *Proc. Natl. Acad. Sci. USA* **110**, 18844–18849 (2013).
46. Farnung, J. et al. Semisynthetic LC3 probes for autophagy pathways reveal a noncanonical LC3 interacting region motif crucial for the enzymatic activity of human ATG3. *ACS Cent. Sci.* **9**, 1025–1034 (2023).
47. Fletcher, K. et al. The WD40 domain of ATG16L1 is required for its non-canonical role in lipidation of LC3 at single membranes. *EMBO J.* **37**, e97840 (2018).
48. Fischer, T. D., Wang, C., Padman, B. S., Lazarou, M. & Youle, R. J. STING induces LC3B lipidation onto single-membrane vesicles via the V-ATPase and ATG16L1-WD40 domain. *J. Cell Biol.* **219**, e202009128 (2020).
49. Cross, J. et al. Lysosome damage triggers direct ATG8 conjugation and ATG2 engagement via non-canonical autophagy. *J. Cell Biol.* **222**, e202303078 (2023).
50. Turco, E. et al. Reconstitution defines the roles of p62, NBR1 and TAX1BP1 in ubiquitin condensate formation and autophagy initiation. *Nat. Commun.* **12**, 5212 (2021).
51. Juris, L. et al. PI3P binding by Atg21 organises Atg8 lipidation. *EMBO J.* **34**, 955–973 (2015).
52. Munzel, L. et al. Atg21 organizes Atg8 lipidation at the contact of the vacuole with the phagophore. *Autophagy* **17**, 1458–1478 (2021).
53. Harada, K. et al. Two distinct mechanisms target the autophagy-related E3 complex to the pre-autophagosomal structure. *eLife* **8**, e43088 (2019).
54. Lewis Kay, E. & Tim Saarinen, P. K. Pure absorption gradient enhanced heteronuclear single quantum correlation spectroscopy with improved sensitivity. *J. Am. Chem. Soc.* **114**, 10663–10665 (1992).
55. Weigelt, J. Single scan, sensitivity- and gradient-enhanced TROSY for multidimensional NMR experiments. *J. Am. Chem. Soc.* **120**, 10778–10779 (1998).
56. Delaglio, F. et al. Nmrpipe—a multidimensional spectral processing system based on unix pipes. *J. Biomol. NMR* **6**, 277–293 (1995).
57. Skinner, S. P. et al. CcpNmr AnalysisAssign: a flexible platform for integrated NMR analysis. *J. Biomol. NMR* **66**, 111–124 (2016).
58. Wang, Z. et al. Automatic crystal centring procedure at the SSRF macromolecular crystallography beamline. *J. Synchrotron Radiat.* **23**, 1323–1332 (2016).
59. Vonrhein, C. et al. Data processing and analysis with the autoPROC toolbox. *Acta Crystallogr. D Biol. Crystallogr.* **67**, 293–302 (2011).
60. Storoni, L. C., McCoy, A. J. & Read, R. J. Likelihood-enhanced fast rotation functions. *Acta Crystallogr. Sect. D Biol. Crystallogr.* **60**, 432–438 (2004).
61. Emsley, P. & Cowtan, K. Coot: model-building tools for molecular graphics. *Acta Crystallogr. Sect. D Biol. Crystallogr.* **60**, 2126–2132 (2004).
62. Adams, P. D. et al. PHENIX: building new software for automated crystallographic structure determination. *Acta Crystallogr. Sect. D Biol. Crystallogr.* **58**, 1948–1954 (2002).
63. Davis, I. W. et al. MolProbity: all-atom contacts and structure validation for proteins and nucleic acids. *Nucleic Acids Res.* **35**, W375–W383 (2007).

## Acknowledgements

The authors thank SSRF BL19U1, BL02U1, and BL10U2 for X-ray beam time, Prof. Jiahuai Han for the full-length WIP12b, ATG8s, FIP200, and ATG16L1 cDNA. This work was supported by grants from the Strategic Priority Research Program of the Chinese Academy of Sciences Grant (No. XDB1060000), the National Natural Science Foundation of China (92253301, 22537007, 22521104), the National Basic Research Program of China (2022YFC2303102), the CAS Youth Interdisciplinary Team (JCTD-2022-10) (to L.P.), and the Postdoctoral Fellowship Program of China Postdoctoral Science Foundation (GZC20232860) (to X.G.).

## Author contributions

X.G. and L.P. designed research; X.G., Yuqian Zhou, Y.W., Y.T., H.L., X.Z., Yuchao Zhang, H.G., and Z.G. performed research; X.G., Yuqian Zhou, and L.P. analyzed data; X.G. and L.P. wrote the paper.

## Competing interests

The authors declare no competing interests.

## Additional information

**Supplementary information** The online version contains supplementary material available at <https://doi.org/10.1038/s41467-025-64097-4>.

**Correspondence** and requests for materials should be addressed to Lifeng Pan.

**Peer review information** *Nature Communications* thanks Nobuo (N) Noda and the other, anonymous, reviewers for their contribution to the peer review of this work. A peer review file is available.

**Reprints and permissions information** is available at <http://www.nature.com/reprints>

**Publisher's note** Springer Nature remains neutral with regard to jurisdictional claims in published maps and institutional affiliations.

**Open Access** This article is licensed under a Creative Commons Attribution-NonCommercial-NoDerivatives 4.0 International License, which permits any non-commercial use, sharing, distribution and reproduction in any medium or format, as long as you give appropriate credit to the original author(s) and the source, provide a link to the Creative Commons licence, and indicate if you modified the licensed material. You do not have permission under this licence to share adapted material derived from this article or parts of it. The images or other third party material in this article are included in the article's Creative Commons licence, unless indicated otherwise in a credit line to the material. If material is not included in the article's Creative Commons licence and your intended use is not permitted by statutory regulation or exceeds the permitted use, you will need to obtain permission directly from the copyright holder. To view a copy of this licence, visit <http://creativecommons.org/licenses/by-nc-nd/4.0/>.

© The Author(s) 2025